Nanoscale spin reversal by non-local angular momentum transfer following ultrafast laser excitation in ferrimagnetic GdFeCo

C. E. Graves[1,2†], A. H. Reid[1,3†], T. Wang[1,4], B. Wu[1,2], S. de Jong[5], K. Vahaplar[3], I. Radu[3,6],
D. P. Bernstein[1,2], M. Messerschmidt[5], L. Müller[7], R. Coffee[5], M. Bionta[5], S. W. Epp[8], R. Hartmann[9],
N. Kimmel[10], G. Hauser[10], A. Hartmann[9], P. Holl[9], H. Gorke[11], J. H. Mentink[3], A. Tsukamoto[12],
A. Fognini[13], J. J. Turner[5], W. F. Schlotter[5], D. Rolles[8], H. Soltau[9], L. Strüder[10], Y. Acremann[13],
A. V. Kimel[3], A. Kirilyuk[3], Th. Rasing[3], J. Stöhr[5], A. O. Scherz[1] and H. A. Dürr[1]★

Ultrafast laser techniques have revealed extraordinary spin dynamics in magnetic materials[1-6] that equilibrium descriptions of magnetism[7] cannot explain. Particularly important for future applications is understanding non-equilibrium spin dynamics following laser excitation on the nanoscale, yet the limited spatial resolution of optical laser techniques has impeded such nanoscale studies. Here we present ultrafast diffraction experiments with an X-ray laser that probes the nanoscale spin dynamics following optical laser excitation in the ferrimagnetic alloy GdFeCo, which exhibits macroscopic all-optical switching[4,8,9]. Our study reveals that GdFeCo displays nanoscale chemical and magnetic inhomogeneities that affect the spin dynamics. In particular, we observe Gd spin reversal in Gd-rich nanoregions within the first picosecond driven by the non-local transfer of angular momentum from larger adjacent Fe-rich nanoregions. These results suggest that a magnetic material's microstructure can be engineered to control transient laser-excited spins, potentially allowing faster ($\sim$1 ps) spin reversal than in present technologies[10-12].

Nanoscale magnetization reversal provides a basis for advanced information technologies, and identifying deterministic switching mechanisms and speed limits is a key challenge. Present technologies driving spin reversal with magnetic fields or voltage-driven spin-polarized currents are limited to timescales of $\sim$100 ps (refs 10–12). This speed limit makes spin reversal by femtosecond optical laser pulses appealing, but in ferromagnets laser excitation typically induces loss of magnetic order[1,13–16]. However, following laser excitation the ferrimagnetic alloy GdFeCo exhibits macroscopic magnetization reversal[4,8,9]. This all-optical switching through inter-sublattice angular momentum transfer[9,17] suggests attractive technological applications if more suitable materials can be engineered to nanoscale dimensions. Whereas an equilibrium understanding of magnetism can explain switching driven by magnetic fields or voltage-driven currents[10–12], it is insufficient to describe laser-excited spin dynamics as the electronic and spin systems are driven quickly into highly non-equilibrium states. In particular, it is critical to understand non-equilibrium spin dynamics on the nanometre length scale where magnetic order emerges. However, the nanoscale spin dynamics and short-range transfer of angular momentum by optically excited electrons[18–24] within the non-equilibrium state of GdFeCo has remained unexplored.
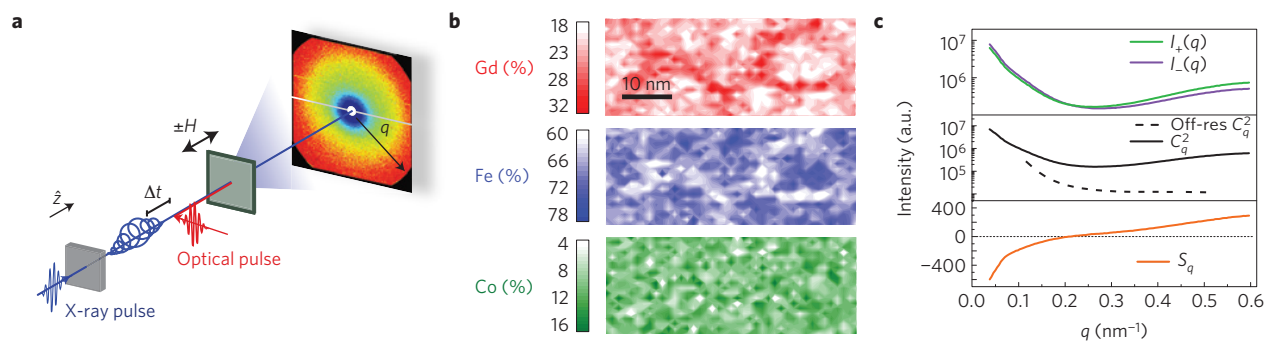
Here we report X-ray laser diffraction measurements that probe the optically excited non-equilibrium spin dynamics on nanometre length scales and femtosecond timescales in GdFeCo (Fig. 1a). We also show that amorphous GdFeCo exhibits chemical and magnetic structure at $\sim$10 nm. We observe the nucleation and transient existence of nanometre-sized regions of Gd spin reversal, before their decay after several picoseconds by thermal fluctuations. This temporally and spatially resolved spin reversal is distinct from the macroscopic magnetization reversal measured previously in this material with spatial-averaging techniques[4,8,9]. Our results reveal a nanoscale flow of angular momentum from Fe spins originating in larger Fe-rich nanoregions to smaller Gd-rich nanoregions. We focus on this non-local transfer by using high optical pump fluences that maximize spin transport while causing overall demagnetization of the sample. In addition, the non-local transfer is highlighted by use of X-ray diffraction, which is spatially sensitive to nanoscale spin variations. We find that non-local angular momentum transfer between Fe $3d$ and Gd $4f$ spins following laser excitation causes Gd spin reversal in Gd-rich nanoregions where this transfer is seemingly amplified.

The macroscopic magnetic state of our sample $Gd_{24}Fe_{66.5}Co_{9.5}$ originates from two distinct sublattices of spins that are antiferromagnetically coupled. The transition metals (Fe and Co)

Figure 1 | Measured chemical and spin inhomogeneity in GdFeCo. Experimental optical-pump X-ray probe geometry with description of measured quantities in scattering and initial nanoscale elemental variance. **a**, Schematic of the magnetic X-ray diffraction experiment. The diffracted intensity is measured as a function of wave vector q, or inverse correlation length. **b**, Local charge nanoscale variations for Gd, Fe and Co in $Gd_{24}Fe_{66.5}Co_{9.5}$ from the same sample region as measured with STEM–EDX. Darker coloured areas indicate elemental enrichment. White denotes below average concentrations. The maps show the anti-correlation of Gd-rich and Fe-rich regions and both Gd and Fe exhibit chemically enriched areas with a frequency of $\sim$10 nm. **c**, Illustration of measured $I_{\pm}(q) = C_q^2 + S_q^2 \pm 2C_q S_q$ data and the separation of C_q and S_q for the Gd $4f$ system. The top panel shows the angle integration of the recorded intensity patterns for parallel and antiparallel orientations of the sample magnetization and beam propagation direction as $I_{+}(q)$ and $I_{-}(q)$. The charge scattering, C_q^2, related to the sum of $I_{\pm}(q)$ (see Methods) is shown in the middle panel, and shows an intensity distribution at a q value ($\sim$0.6 nm^{-1}) in line with the chemical enrichment periodicity ($\sim$10 nm) observed in **b**. We also show the C_q^2 off-resonance (Off-res) data as a dashed line for comparison. S_q, the Fourier component of the spin distribution in the sample, related to the difference of $I_{\pm}(q)$ (see Methods) is shown in the bottom panel. The intensity distribution of S_q at $q \sim 0.6$ nm^{-1} indicates the coexistence of spin variation with the chemically enriched regions shown in **b**.

provide one sublattice, which consists of both atomic $3d$ and mobile s–p spins, and the rare-earth metal Gd gives rise to a second sublattice with oppositely aligned spins mainly localized in the $4f$ shell. Although GdFeCo is widely considered a homogeneous amorphous alloy, we find that at nanometre length scales the material's chemical homogeneity is broken by chemical segregation. The local elemental variations for Gd, Fe and Co are shown in Fig. 1b, as measured by scanning transmission electron microscopy (STEM) with elemental sensitivity from energy-dispersive X-ray spectroscopy (EDX). This characterization yields the surprising result of nanoscale chemical inhomogeneity, and the question remains how this local structure affects the spin subsystems. We address this question using soft X-ray scattering, and therefore shift from mapping real space to probing reciprocal space.

The X-ray scattering experimental set-up is shown schematically in Fig. 1a. Circularly polarized X-rays selectively detect the Fe $3d$ and Gd $4f$ spins by resonantly exciting core electrons into their respective spin shell (see Methods and Supplementary Information). Incident X-rays are transmitted non-uniformly owing to local modulations of the X-ray absorption by the chemically inhomogeneous sample (Fig. 1b). The resulting X-ray diffraction patterns consist of linear combinations of reciprocal-space Fourier amplitudes C_q and S_q of the sample's chemical and magnetic real-space distributions[23–25]. Figure 1c shows the angle-integrated intensity $I_{\pm}(q)$ of Gd $4f$ diffraction patterns taken with circularly polarized resonant X-rays as a function of wave vector, q, for opposite initial magnetic states (top panel). C_q and S_q can be seprated from these data using $I_{\pm}(q) = |C_q \pm S_q|^2$ (ref. 26), and are shown in the middle and bottom panels.

C_q is the Fourier amplitude of the spatial chemical distribution within the sample (see Fig. 1c for an example). A perfectly homogeneous sample would give an $I_{\pm}(q)$ signal principally at $q = 0$. Amplitudes in C_q and S_q away from $q = 0$ indicate the presence of variations in the real-space charge and spin distributions, as q corresponds to the inverse correlation length. $I_{\pm}(q)$ would simply decrease with q, as shown by the dashed line in Fig. 1c, if film thickness changes were the only variations present in the sample. However, the Gd C_q (solid line) of our sample clearly deviates from this monotonous behaviour, owing to the Gd-enriched areas shown in Fig. 1b. The C_q local scattering maximum at $\sim$0.6 nm^{-1} corresponds to a correlation length of $\sim$10 nm for Gd-rich areas,

in excellent agreement with the real-space data. A similar C_q distribution results from Fe chemical enrichment, peaking at a q value corresponding to a correlation length of $\sim$13 nm (see Supplementary Sections S1.2 and S2.2). These results show that the sample segregates into Gd-rich ($\sim$20% of the sample) and Fe-rich nanoregions ($\sim$40% of the sample), which are spatially anti-correlated (Fig. 2a).

Chemical segregation into Gd-rich and Fe-rich nanoregions alters the sublattice spin distributions, which are measured by S_q, the magnetic Fourier amplitude. S_q measures the deviation of local magnetic moments from the average sublattice magnetization. Equilibrium distributions of S_q are shown in the top row of Fig. 2b with Gd S_q in red and Fe S_q in blue. The S_q distributions of the two sublattices show opposite magnetization directions, as expected for a ferrimagnet[8]. There are two distinct contributions to S_q for both Gd and Fe. Film thickness variations dominate for low-q values ($q < 0.2$ nm^{-1}), and the integration of this contribution is identical to the signal obtained with spatial averaging techniques[8] (see Supplementary Information). However, magnetic variations associated with the chemical segregation of the enriched regions dominate at high-q values ($q > 0.2$ nm^{-1}, shaded). The opposite sign of S_q in the high-q region indicates the anti-correlation of the charge and spin distributions: chemically enriched areas simultaneously exhibit a reduction in M_z of the enriched element. By modelling the high-q S_q contributions, we obtain the reconstructed real-space magnetization M_z values in the chemically enriched regions (see Methods and Supplementary Section S2.3). M_z values for Gd and Fe sublattices are illustrated in the centre column of Fig. 2b as red and blue arrows. The local M_z of the enriched element is reduced in both the Gd-rich and Fe-rich nanoregions as compared with the average: ΔM_z^{Gd} is -7.8 μ_B nm^{-3} in Gd-rich and ΔM_z^{Fe} is -1.1 μ_B nm^{-3} in Fe-rich regions. These values indicate that local changes in the Gd magnetization are much larger than those in the Fe magnetization.

To probe the dynamic behaviour of ΔM_z following laser excitation, we measure the S_q distributions, which are proportional to ΔM_z, for different time delays Δt (shown in Fig. 2b). The femtosecond laser excitation deposits energy directly into the $3d$ electron system, subsequently generating mobile s–p spins[18] without exciting the $4f$ spins[15]. The low-q and high-q S_q contributions in Fig. 2b exhibit clearly different time characteristics.
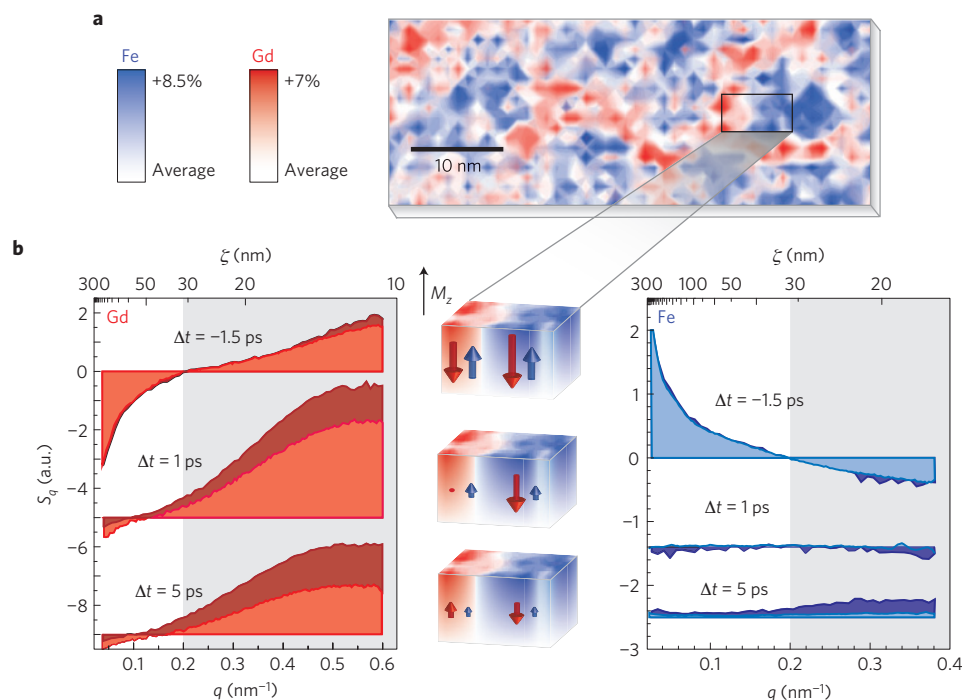
Figure 2 | Nanoscale variations in charge and spin distributions drive q-dependent magnetic scattering dynamics. a, Concentration map for Gd and Fe from STEM–EDX data taken on $Gd_{24}Fe_{66.5}Co_{9.5}$ (shown in Fig. 1b). Red areas indicate a local enrichment of Gd atoms and blue areas indicate a local enrichment of Fe atoms, with enrichment defined as a deviation higher than 3% above average (white shading). These data in combination with the X-ray scattering data give the average local variation in elemental concentration as 5.1% for Gd-enriched areas and 1.9% for Fe-enriched areas. Furthermore, Gd-rich nanoregions cover ∼20% of the sample, and Fe-rich nanoregions cover ∼40% of the sample (see Supplementary Information). **b**, Magnetic X-ray diffraction, S_q, of Gd 4f and Fe 3d versus wave vector, q, and $\zeta = 2\pi/q$, for the indicated X-ray delay times, Δt. The darker shaded areas show data with 16 mJ cm^{-2} and lighter shaded areas show data with 24 mJ cm^{-2} optical pump fluence. The thermalized temperature at 1 ps for both fluences is above the critical temperature, T_c. Negative time refers to equilibrium conditions before optical excitation. The data were averaged over 1 ps intervals around the indicated delays and are offset vertically for clarity. The high-q scattering ($q > 0.2$ nm^{-1}) from the chemically enriched regions shown in **a** is shaded grey. Illustrated between the two plots is the calculated local variation in the spin distribution M_z within the Gd- and Fe-rich regions for 24 mJ cm^{-2} pump fluence.

Whereas the low-q S_q scattering (average sample magnetization) decays with time, the high-q S_q contribution increases for Gd and changes sign for Fe. The low-q and high-q S_q behaviour is shown in more detail for smaller time delay steps in Fig. 3. The low-q S_q data in the top panel of Fig. 3a,b reflect the quenching of the average Gd and Fe sublattice magnetizations. S_q for Fe and Gd decays with time constants of 320 ± 50 fs and 570 ± 50 fs respectively, values typical for demagnetization[16]. In addition to the high-q S_q differences noted above, the bottom panel of Fig. 3a,b reveals that both high-q responses are delayed by 360 ± 50 fs. The S_q response following laser excitation is more clearly illustrated by the reconstructed local magnetization M_z for Fe- and Gd-rich nanoregions (see Methods and Supplementary Information), shown in Fig. 3c. In Fe-rich nanoregions, both sublattices exhibit demagnetization, which is also observed macroscopically (see Supplementary Information). However, the Gd-rich nanoregions respond differently: M_z^{Gd} of the Gd-rich regions reverses sign at $\Delta t \sim 1$ ps. As M_z^{Fe} maintains its sign, a net ferromagnetic alignment of the two sublattice magnetizations occurs within the Gd-rich nanoregions after ∼1 ps and persists several picoseconds thereafter. At 2 ps, the Gd spins in Gd-rich nanoregions have reversed from their initial value of $-73\ \mu_B$ nm^{-3} to $+10.7 \pm 6.4\ \mu_B$ nm^{-3}. This angular momentum transfer is surprisingly enhanced at lower optical pump fluences: with 16 mJ cm^{-2} pump fluence, the Gd spins in Gd-rich nanoregions show a reversed value of $+49.3 \pm 14.0\ \mu_B$ nm^{-3} after 2.5 ps. As the local change ΔM_z^{Gd} is much greater than ΔM_z^{Fe}, non-local angular momentum transfer to Gd spins within Gd-rich nanoegions is required.

Analysis of the high-q S_q dynamics quantifies the amount of non-local angular momentum transfer to the Gd-rich nanoregions. The high-q S_q measures the local difference of the sublattice magnetizations from the average, or ΔM_z, within the enriched regions. Whereas ΔM_z^{Gd} increases with time, the ΔM_z^{Fe} becomes smaller, revealing non-local angular momentum transfer to the Gd-rich regions' M_z^{Gd}, as otherwise ΔM_z^{Fe} would necessarily be larger. The non-local transfer is characterized by J_S, the time evolution of the net angular momentum flow into the Gd-rich nanoregions, shown in Fig. 3d. J_S is the rate of change of ΔM_z or $J_S = d/dt (\Delta M_z)_{Gd-rich} = d/dt (\Delta M_z^{Gd} + \Delta M_z^{Fe})_{Gd-rich}$ and is dominated by the Gd contribution because $d/dt (\Delta M_z^{Gd})_{Gd-rich} \gg d/dt (\Delta M_z^{Fe})_{Gd-rich}$. Within 1 ps, a net $14\ \mu_B$ nm^{-3} is transferred to the Gd-rich nanoregions. Moreover, the positive sign of J_S during the first picosecond indicates that it is the Fe spins that transport angular momentum into the Gd-rich nanoregions, as only they possess the correct sign. After 1 ps, J_S becomes negative indicating a slower back-flow of angular momentum out of the Gd-rich regions. This backflow continues until between 4 and 6 ps when the Gd magnetization switches back and the ground-state ferrimagnetism is re-established.

It is important to consider why the non-local transfer of angular momentum leads to Gd spin reversal specifically within the disordered Gd-rich nanoregions. Following optical excitation, Fe 3d spins are excited into s–p states[18,21,27], and angular momentum then moves from Fe to various reservoirs: the local Gd reservoir, the lattice[16] and non-local transport[18,19,21–24]. Previous work on GdFeCo focused on the macroscopic angular momentum transfer
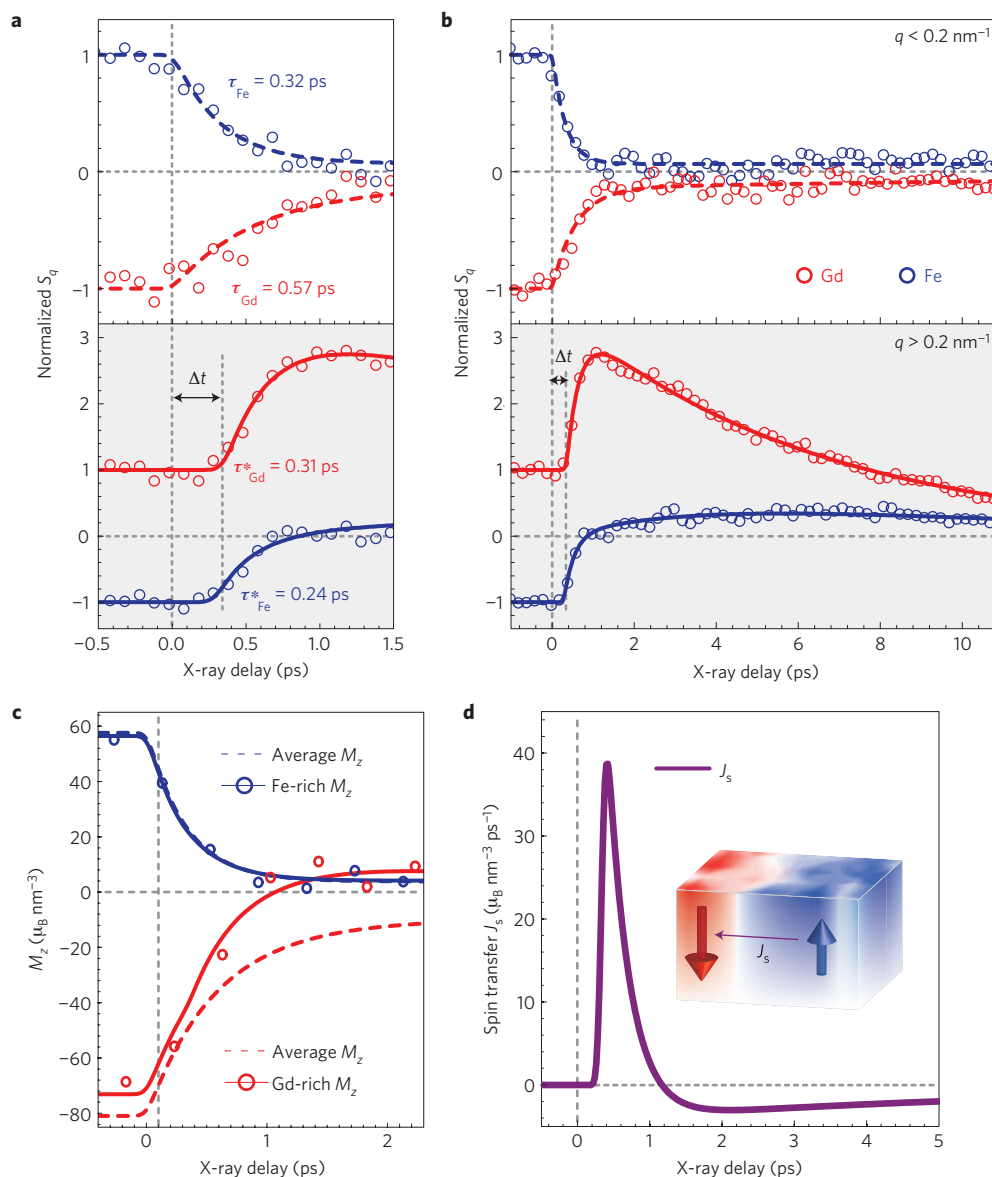
Figure 3 | Reversal of Gd spins within nanoscale Gd-rich regions as measured by resonant X-ray diffraction a, Temporal evolution of magnetic diffraction, S_q, for Gd $4f$ (red) and Fe $3d$ (blue) spins measuring the local deviations from the average magnetization. **b**, The same as in **a** but on a 10 ps timescale. S_q signals were integrated over the low-q (top panel, $q < 0.2$ nm^{-1}) and grey shaded high-q (bottom panel, $q > 0.2$ nm^{-1}) regions of Fig. 2b,c and are normalized to the equilibrium values. Normalized $|S_q(t<0)| = 1$ for both q-ranges and sublattices, although high-q S_q for Gd is ~4 times greater than for Fe. Dashed and solid lines represent fits of exponential decay and rise functions to the data, respectively[8,14,15]. The observed delayed onset at $\Delta t = 360 \pm 50$ fs indicates that the non-local angular momentum transfer effectively occurs only after this time delay. The subsequent Gd and Fe rise times of 310 ± 100 and 240 ± 100 fs, respectively, are essentially identical. Beyond 1 ps, the Gd (Fe) data are well described by an exponential decay (rise) with a time constant of 6 ± 2 ps. The Fe data are fitted with an additional decay with time constant 8 ps. **c**, Time evolution of M_z in the Gd-rich and Fe-rich regions compared with the sample average. Solid lines are calculated from the fits in **a**; data points are averaged from data in **a**. **d**, Time-resolved angular momentum flow, J_s, into the Gd-rich regions. The plot shows a time-delayed spike in the angular momentum transfer to the Gd spins in the Gd-rich nanoregions that lasts ~1 ps. Following this spin transfer to the Gd-rich nanoregions, a slower and weaker dissipation of spin from the region occurs.

observed at lower fluences[8,17]. In contrast, our measurements isolate the nanoscale spatial variations of this transfer. In addition, we observe Gd spin reversal, not Fe, contrary to reported local theories of non-equilibrium dynamics[9,17], and we observe the spin reversal in regions of Fe depletion where even less Fe angular momentum is available to transfer locally. Transfer of angular momentum from Fe to Gd occurs through the exchange interaction. This transfer is enhanced within the Gd-rich regions owing not only to local enhancement of the Gd–Fe exchange, but also to spin-torque scattering at the interface of the Gd-rich regions resulting from non-collinear spins and abrupt chemical variations on the electron

scattering length scale[28,29]. Surprisingly, this spin transfer has a delayed onset, suggesting a threshold-like behaviour. Although the observed spin transfer and reversal could be due to spin currents[18,21,23,24], the presence of the delay indicates the need for further theoretical work. The spin transfer to the Gd-rich regions peaks around ~1 ps, a timescale characteristic for hot electrons to reach thermal equilibrium with the lattice[1,4,27]. Growth of the reversed Gd-rich regions is indicated by the shift of the S_q maximum to lower q values with increasing delay time, characteristic of a size increase of the spin-reversed area[30]. The reversed Gd magnetization dissipates following the spin transfer, proceeding through Fe spin

states, as demonstrated by the fact that the increase of Fe and the decrease of Gd ΔM_z have the same time constant.

By measuring nanometre–femtosecond spin scattering dynamics that are accessible only with X-ray lasers, we demonstrate nanoscale spin reversal in GdFeCo driven by non-local transfer of angular momentum. Our experimental technique opens a new way to study emerging phenomena, such as order in highly non-equilibrium systems. Our results not only link two important present fields in spintronics, namely transport and ultrafast optics, but also point to the general importance of nanoscale inhomogeneities in the study of many fundamental phenomena, such as crystal growth, the role of fluctuations in high-T_c superconductors and the emergence of quantum electronic phases hidden in thermal equilibrium. The observed angular momentum transfer reverses spins robustly and overcomes the magnetic disorder, suggesting an effective tool for controlling laser-excited spins in microscopically engineered magnetic materials. Furthermore, the observed spin reversal is orders of magnitude faster than reversal by conventional voltage-driven equilibrium spin currents and may offer marked improvements over present spin-torque devices.

Methods

The studied sample was a 30 nm $Gd_{24}Fe_{66.5}Co_{9.5}$ amorphous out-of-plane magnetized thin film deposited by magnetron sputtering on a 100 nm Si_3N_4 membrane, similar to those used in ref. 8. To protect the GdFeCo layer and prevent oxidation, 5 nm and 10 nm of Si_3N_4 were used as buffer and capping layers respectively.

Time-resolved X-ray scattering measurements were performed in transmission mode in a collinear pump–probe geometry. Samples were photoexcited by a 50 fs optical laser pulse ($\lambda = 800$ nm) at 16 and 24 mJ cm^{-2}, and probed with 80 fs circularly polarized X-ray pulses at the Fe L_3 (707 eV) and Gd M_5 (1,189 eV) edges, enabling an independent probe of Gd and Fe atoms. The X-ray pulses were passed through a thin magnetic film to produce circular polarization. Single-shot X-ray diffraction patterns were recorded by a high-frame-rate, low-noise X-ray pn-CCD (charge-coupled device) detector at the Linac Coherent Light Source repetition rate of 60 Hz. In between pump–probe events, the sample was reset by an external magnetic field (± 0.3 T) in alternating opposite directions. The diffracted intensity $I_+(q)$ and $I_-(q)$ were recorded at fixed X-ray helicity and opposite resetting magnetic field as a function of pump–probe delay. As incident X-rays are transmitted by the sample nonuniformly owing to local modulations in the sample, the resulting X-ray diffraction pattern contains the Fourier components C_q and S_q of the chemical and magnetic real-space distributions respectively. The intensity of the diffracted X-rays can therefore be written as $I_{\pm}(q) = C_q^2 + S_q^2 \pm 2C_q S_q$. We analyse the transient evolution of S_q to isolate the magnetic response of the sample, which can be written as $S_q = 1/\sqrt{(8)} * (I_+ - I_-)/\sqrt{(I_+ + I_-)}$ with some approximations (see Supplementary Information).

Elemental mapping of the nanoscale chemical variations of Gd and Fe was performed with an EDX detector in STEM mode with a probe size of ∼1 nm. All STEM–EDX measurements used an FEI Tecnai G2 F20 X-TWIN TEM with an EDAX SUTW (super ultrathin window) and analyser. Measurements were performed on a 30 nm $Gd_{24}Fe_{66.5}Co_{9.5}$ sample grown on an 8 nm Si_3N_4 STEM grid. The nominal and measured average concentrations were found to agree within 0.8%.

Calculations of the time-evolution local variations in M_z used weight factors γ_{Fe} and γ_{Gd} for the magnetic changes in the respective Fe- and Gd-enriched regions derived from equilibrium data and modelling. These factors give the local change in the magnetization with respect to the sample average within these regions. The magnetization at any point can be described by $M_z(x,y) = M_z^{average} + \Delta M_z(x,y)$. As the S_q distribution at high-q is proportional to ΔM_z, $\Delta M_z^{Gd} = \gamma_{Gd} * S_q^{Gd}(q > 0.2 \text{ nm}^{-1})$, the size of M_z in the chemically enriched areas can be calculated from the S_q data. The net spin flow into the Gd-enriched regions, J_s, is defined as the rate of change of ΔM_z or $J_S = \partial/\partial t (\Delta M_z^{Gd} + \Delta M_Z^{Fe})_{\text{Gd-rich}} = \partial/\partial t (\gamma_{Gd} S_{q>0.2 \text{ nm}^{-1}}^{Gd} + \gamma_{Fe} S_{q>0.2 \text{ nm}^{-1}}^{Fe})_{\text{Gd-rich}}$ and the dominant contribution is from Gd as $\partial/\partial t (\gamma_{Gd} S_{q>0.2 \text{ nm}^{-1}}^{Gd})_{\text{Gd-rich}} \gg \partial/\partial t (\gamma_{Fe} S_{q>0.2 \text{ nm}^{-1}}^{Fe})_{\text{Gd-rich}}$. Therefore, J_s (as shown in Fig. 3d) is calculated from the high-q S_q data shown in the bottom panels of Fig. 3a,b. The total angular momentum transferred into the Gd-rich regions during the first picosecond is calculated by integrating J_s.

References

1. Beaurepaire, E., Merle, J-C., Daunois, A. & Bigot, J-Y. Ultrafast spin dynamics in ferromagnetic nickel. *Phys. Rev. Lett.* **76,** 4250–4253 (1996).
2. Bigot, J-Y., Vomir, M. & Beaurepaire, E. Coherent ultrafast magnetism induced by femtosecond laser pulses. *Nature Phys.* **5,** 515–520 (2009).
3. Ju, G. *et al.* Ultrafast generation of ferromagnetic order via a laser-induced phase transformation in FeRh thin films. *Phys. Rev. Lett.* **93,** 197403 (2004).
4. Stanciu, C. D. *et al.* All-optical magnetic recording with circularly polarized light. *Phys. Rev. Lett.* **99,** 047601 (2007).
5. Kirilyuk, A., Kimel, A. & Rasing, Th. Ultrafast optical manipulation of magnetic order. *Rev. Mod. Phys.* **82,** 2731–2784 (2010).
6. Guidoni, L., Beaurepaire, E. & Bigot, J-Y. Magneto-optics in the ultrafast regime: Thermalization of spin populations in ferromagnetic films. *Phys. Rev. Lett.* **89,** 17401 (2002).
7. Stöhr, J. & Siegmann, H. C. *Magnetism: From Fundamentals to Nanoscale Dynamics* (Springer, 2006).
8. Radu, I. *et al.* Transient ferromagnetic-like state mediating ultrafast reversal of antiferromagnetically coupled spins. *Nature* **472,** 205–208 (2011).
9. Ostler, T. *et al.* Ultrafast heating as a sufficient stimulus for magnetization reversal in a ferrimagnet. *Nature Commun.* **3,** 666 (2012).
10. Back, C. H. *et al.* Minimum field strength in precessional magnetization reversal. *Science* **285,** 864–867 (1999).
11. Acremann, Y. *et al.* Time-resolved imaging of spin transfer switching: Beyond the macrospin concept. *Phys. Rev. Lett.* **96,** 217202 (2006).
12. Slonczewski, J. C. Current-driven excitation of magnetic multilayers. *J. Magn. Magn. Mater.* **159,** L1–L7 (1996).
13. Koopmans, B., Van Kampen, M., Kohlhepp, J. T. & de Jonge, W. J. M. Ultrafast magneto-optics in nickel: Magnetism or optics? *Phys. Rev. Lett.* **85,** 844–847 (2000).
14. Stamm, C. *et al.* Femtosecond modification of electron localization and transfer of angular momentum in nickel. *Nature Mater.* **6,** 740–743 (2007).
15. Wietstruk, M. *et al.* Hot-electron-driven enhancement of spin-lattice coupling in Gd and Tb 4*f* ferromagnets observed by femtosecond X-ray magnetic circular dichroism. *Phys. Rev. Lett.* **106,** 127401 (2011).
16. Koopmans, B. *et al.* Explaining the paradoxical diversity of ultrafast laser-induced demagnetization. *Nature Mater.* **9,** 259–265 (2010).
17. Mentink, J. H. *et al.* Ultrafast spin dynamics in multisublattice magnets. *Phys. Rev. Lett.* **108,** 057202 (2012).
18. Battiato, M., Carva, K. & Oppeneer, P. M. Superdiffusive spin transport as a mechanism of ultrafast demagnetization. *Phys. Rev. Lett.* **105,** 027203 (2010).
19. Melnikov, A. *et al.* Ultrafast transport of laser-excited spin-polarized carriers in Au/Fe/MgO(001). *Phys. Rev. Lett.* **107,** 076601 (2011).
20. Malinowski, G. *et al.* Control of speed and efficiency of ultrafast demagnetization by direct transfer of spin angular momentum. *Nature Phys.* **4,** 855–888 (2008).
21. Battiato, M., Carva, K. & Oppeneer, P. M. Theory of laser-induced ultrafast superdiffusive spin transport in layered heterostructures. *Phys. Rev. B* **86,** 024404 (2012).
22. Rudolf, D. *et al.* Ultrafast magnetization enhancement in metallic multilayers driven by superdiffusive spin current. *Nature Commun.* **3,** 1037 (2012).
23. Vodungbo, B. *et al.* Laser-induced ultrafast demagnetization in the presence of a nanoscale magnetic domain network. *Nature Commun.* **3,** 999 (2012).
24. Pfau, B. *et al.* Ultrafast optical demagnetization manipulates nanoscale spin structure in domain walls. *Nature Commun.* **3,** 1100 (2012).
25. Gutt, C. *et al.* Single-pulse resonant magnetic scattering using a soft X-ray free-electron laser. *Phys. Rev. B* **81,** 100401 (2010).
26. Hannon, J. P., Trammell, G. T., Blume, M. & Gibbs, D. X-ray resonance exchange scattering. *Phys. Rev. Lett.* **61,** 1245–1248 (1988).
27. Rhie, H-S., Dürr, H. A. & Eberhardt, W. Femtosecond electron and spin dynamics in Ni/W(110) films. *Phys. Rev. Lett.* **90,** 247201 (2003).
28. Stiles, M. D. & Zangwill, A. Anatomy of spin-transfer torque. *Phys. Rev. B* **66,** 014407 (2002).
29. Bass, J. & Pratt, W. P. Spin diffusion lengths in metals and alloys, and spin-flipping at metal/metal interfaces: An experimentalist's critical review. *J. Phys. Condens. Matter* **19,** 183201 (2007).
30. Zuo, J-K., Wendelken, J. F., Dürr, H. & Liu, C-L. Growth and coalescence in submonolayer homoepitaxy on Cu(100) studied with high-resolution low-energy electron diffraction. *Phys. Rev. Lett.* **72,** 3064–3067 (1994).

Author contributions

Additional information

Competing financial interests